What is Multi-extreme THz ESR? Developments and its Applications

Ohta, Hitoshi
Okubo, Susumu
Ohmichi, Eiji
Takahashi, Hideyuki
Sakurai, Takahiro

(Citation)
Applied Magnetic Resonance,56(1):33-55

(Issue Date)
2025-02

(Resource Type)
journal article

(Version)
Version of Record

(URL)
https://hdl.handle.net/20.500.14094/0100491876

Applied Magnetic Resonance
https://doi.org/10.1007/s00723-024-01722-3

Applied
Magnetic Resonance

REVIEW

What is Multi-extreme THz ESR? Developments and its Applications

H. Ohta[1] · S. Okubo[1,2] · E. Ohmichi[2] · H. Takahashi[1] · T. Sakurai[3]

Received: 10 June 2024 / Revised: 26 September 2024 / Accepted: 8 October 2024

Abstract
This review explores the multi-extreme THz ESR system in Kobe, Japan, with a focus on pulsed magnetic fields, mechanical detection, and high pressure as central elements of multi-extreme THz ESR. Initially, it discusses the advantages of multi-frequency THz ESR using mini-pulsed and 55 T−pulsed magnetic fields, with typical examples featuring the finite Haldane chain substance $Y_2BaNi_{0.96}Mg_{0.04}O_5$ and the deformed diamond chain antiferromagnet $Cu_3(CO_3)_2(OH)_2$ (Azurite). The measurement efficiency and the measurement beyond the magnetic phase transition, in contrast to the conventional superconducting magnet, are discussed. Second, the high sensitivity obtained from the use of a nano-membrane for mechanical detection is shown. Also shown are the high-temperature (280 K) THz ESR results for DPPH powder and a $Cu(C_4H_4N_2)(NO_3)_2$ (CuPzN) single crystal, with the combination of a nano-membrane device and a high-power source, a gyrotron. Finally, the high-pressure THz ESR results for $KCuCl_3$ using a transmission-type double-layered pressure cell are shown, along with the application of the thermally detected high-pressure THz ESR.

1 Introduction

Our group in Kobe, Japan, has been developing THz ESR for over 37 years. Here, the definition of "THz" in the THz community corresponds to 0.1−10 THz [1]. On the other hand, the resonance condition of ESR is

$$h\nu = g\mu_B H \tag{1}$$

✉ H. Ohta
hohta@kobe-u.ac.jp

[1] Molecular Photoscience Research Center, Kobe University, Kobe 657-8501, Japan

[2] Graduate School of Science, Kobe University, Kobe 657-8501, Japan

[3] Research Facility Center for Science and Technology, Kobe University, Kobe 657-8501, Japan

Published online: 25 October 2024

where h is the Planck constant, ν is the frequency of the electromagnetic wave, g is the g value, μ_B is the Bohr magneton, and H is the applied magnetic field where the unit of H is Tesla. In the conventional X-band ESR system operating around 9.5 GHz, and the resonance field of EPR ($g=2$) is about 0.339 T, where the magnetic field is usually applied by a water-cooled resistive magnet. However, the frequencies beyond the W-band ($\nu > 95$ GHz) necessitate a superconducting magnet, where the conventional superconducting magnets are limited to 20 T in the conventional laboratory level. According to Eq. (1) for $g=2$, 20 T corresponds to 560 GHz. Therefore, the frequencies beyond 560 GHz requires a specialized technique for magnetic field application, as discussed in the next section.

To observe the electron paramagnetic resonance (EPR) of radicals, the necessity of developing THz ESR instead of X-band ESR might not be immediately apparent, given the high magnetic fields required for high-frequency EPR, as explained above. However, THz ESR has several advantages over X-band ESR, as listed below [2].

1) As we are mainly dealing with 3d ions and strongly correlated magnetic systems, the first advantage is the enhanced ESR absorption intensity at higher frequencies, since this intensity increases proportionally to $(1-\exp(-\Delta E/k_B T))$, where k_B is the Boltzman constant and T is the temperature, in relation to the distribution disparity in the Zeeman splitting ΔE. For instance, the intrinsic intensity of ESR is much higher than that of NMR. However, this advantage is usually counterbalanced by the reduction in the output power of conventional light sources such as Gunn oscillators or backward-traveling wave oscillators (BWO) with increasing frequency.
2) The next advantage pertains to the spectral resolution. ESR or EPR exhibits linewidth characteristics. When dealing with two EPR spectra with very closely positioned g values, the two EPRs are indistinguishable if $\Delta g \mu_B H$ is smaller than the linewidth. However, at high frequencies, two EPRs will separate because $\Delta g \mu_B H$ exceeds the linewidth due to the increase in the resonance field.
3) If the ESR exhibits zero-field splitting, observing ESR requires frequencies exceeding the zero-field splitting. Certain 3d metal ions, such as Fe^{3+} ($3d^5$) in Hemin (zero-field splitting = 400 GHz), demonstrate zero-field splitting, necessitating multi-frequency THz ESR for its observation and understanding, as shown in Fig. 1 [3, 4]. Antiferromagnetic resonance (AFMR) resonance fields expand extensively from EPR due to antiferromagnetic gap induced by internal fields from antiferromagnetic order below the Néel temperature T_N. Multi-frequency THz ESR is a powerful method for observing AFMR, exemplified by Li_2CuO_2 with $T_N = 9.3$ K, as shown in Fig. 2 [5].
4) In magnetic systems undergoing a magnetic phase transition at H_m, it is necessary to adjust multi-frequencies to place the resonance field above H_m to study the magnetic phase ($H > H_m$). Figure 3 shows the discontinuous change of AFMR in $CsCuCl_3$ [10] at H_m, which is interpreted as the competition between the weak in-plane magnetic anisotropy and the quantum effect by the Nikuni–Shiba theory [11].

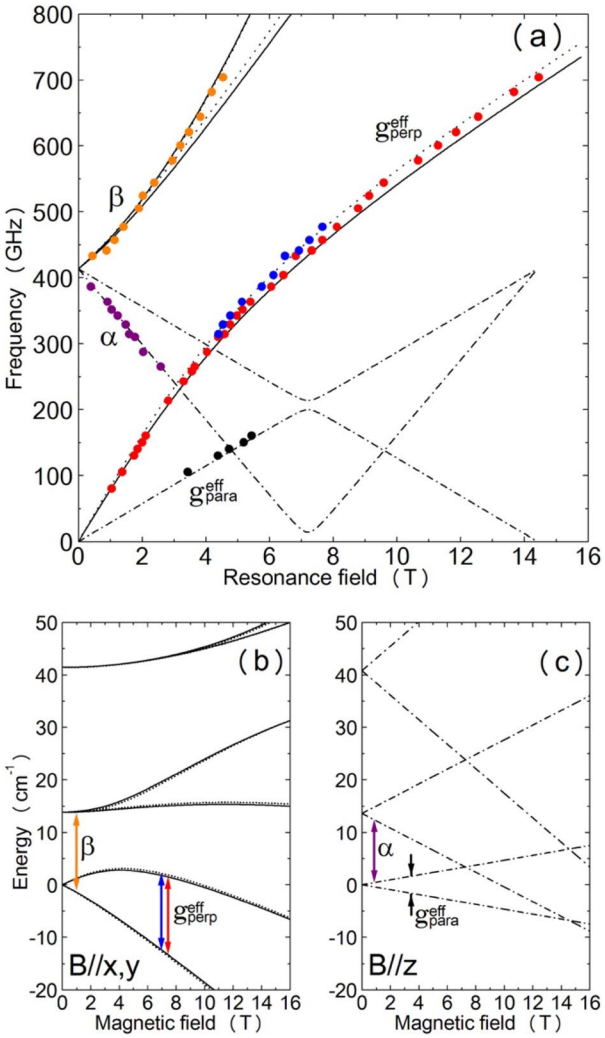

Fig. 1 **a** Electromagnetic-wave frequency versus resonance field derived from the observed EPR spectra for a powder sample of hemin, together with simulated curves, taking into account ZFS parameters. **b** Calculated energy levels of hemin for B // x, y, and vertical arrows indicate the corresponding EPR transitions for the field-swept data at 441 GHz. Curves for B // x and y are almost overlapped and cannot be resolved in this scale. **c** Calculated energy levels of hemin for B // z. Purple (α) and black (g^{eff}_{para}) arrows indicate the corresponding EPR transitions for the field-swept data at 363 and 105 GHz, respectively [3]. Reproduced with permission from Ref. [3]. **c** (2018) The Physical Society of Japan

5) To observe a broad ESR line, THz ESR is required. Since 3d metallic ions have much broader ESR linewidths compared to those of radicals, THz ESR is useful for observing systems containing 3d metallic ions. Figure 4 shows the ESR with a linewidth of several Tesla in $SrCr_8Ga_4O_{19}$, which is due to the strong spin frustration in the system [12].

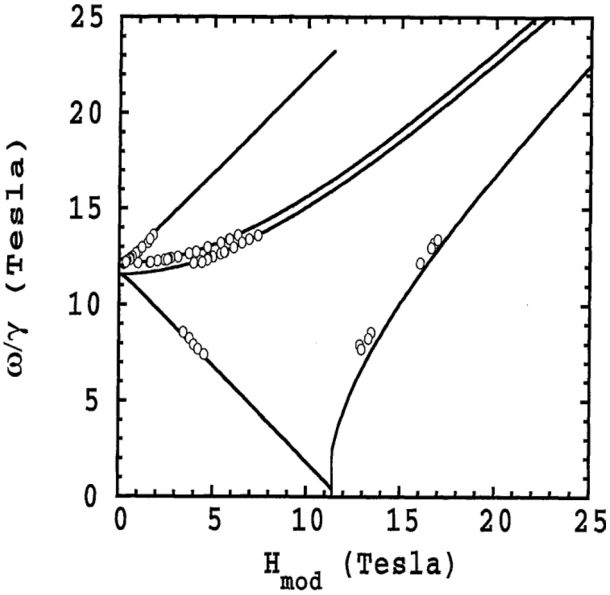

Fig. 2 Frequency-field diagram of observed AFMR's (open circles) of Li_2CuO_2 powder sample at 1.9 K. $\omega/\gamma = 10$ T in the vertical axis corresponds to 280 GHz. Modified field H_m corresponds to (g $H_{exp}/2$), where H_{exp} is the experimentally obtained resonance field. Solid lines are calculated by the AFMR theory based on the molecular field theory [5]. Reproduced with permission from Ref. [5]. (c) (1993) The Physical Society of Japan

This THz ESR system in Kobe has been extended to encompass the multi-extreme THz ESR [13]. Our multi-extreme THz ESR covers the frequency range from 0.03 to 7 THz using Gunn oscillators, multipliers, BWOs and far-infrared (FIR) laser [14], the temperature range from 1.8 to 300 K [14], the magnetic field intensities up to 55 T [14], and the pressure is increased from 1.5 GPa [15] to 2.5 GPa using a hybrid-type pressure cell [16–18]. It also includes our recent developments of mechanically detected THz ESR [19] measurements using a commercially available membrane-type surface stress sensor, an extension of our micro-cantilever ESR [20, 21], and its application to microliter solution samples such as myoglobin [22]. This review presents our high magnetic field THz ESR, the mechanically detected THz ESR and the high-pressure THz ESR, and the reader is encouraged to refer to cited articles to obtain more information.

2 High Magnetic Field THz ESR

To apply the magnetic fields for THz ESR, either steady magnetic fields or the pulsed magnetic fields can be used. The disadvantage of steady magnetic fields using a superconducting magnet lies in the sweep time. It typically takes about 25 min to sweep a superconducting magnet from 0 to 15 T. However,

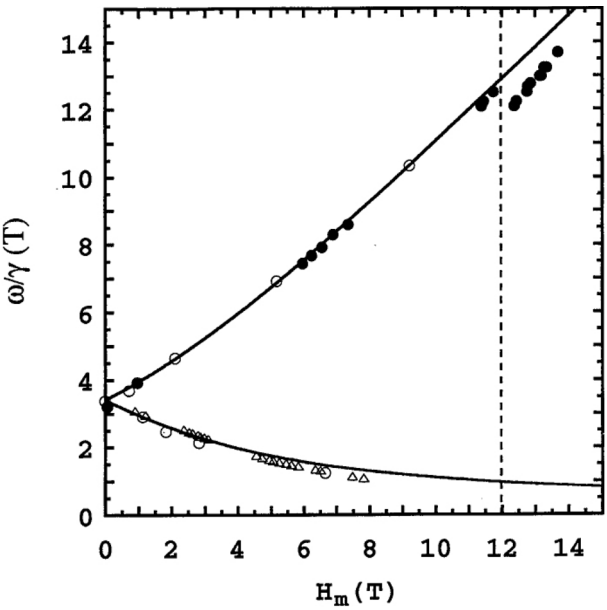

Fig. 3 Frequency-field diagram of $CsCuCl_3$ for H//c at 4.2 K. $\omega/\gamma = 10$ T in the vertical axis corresponds to 280 GHz. Modified field H_m corresponds to (g $H_{exp}/2$), where H_{exp} is the experimentally obtained resonance field. Here, the g value of 2.10 obtained from our EPR measurements is used for H_m. The results of our THz ESR (closed circles) are shown with the results of Palme et al. (open circles) [6] and the AFMR calculated results based on the molecular field theory by Tanaka et al. (solid lines) [7]. ESR results obtained by Motokawa [8] in the low frequency region at 1.4 K are also shown by the open triangles. The dashed line corresponds to the critical field $H_{c1} = 11.4$ T obtained from the magnetization measurement [9]. Clear discontinuous change of ESR mode is observed at H_{c1} [10]. Reproduced with permission from Ref. [10]. **c** (1993) The Physical Society of Japan

our mini-pulsed magnetic field system shown in Fig. 5 requires only 10 ms to sweep from 0 to 15 T [23]. Here, the light sources are far-infrared (FIR) laser and backward traveling wave oscillators (BWO or BTWT) before 1995, and Gunn oscillators and multipliers became available after 1995. A pulsed magnetic field is produced by an LC-circuit, which consists of a mini-coil and a 35 kJ (3 kV) capacitor bank. Therefore, a pulsed magnetic field shows a sinusoidal field profile as a function of time. In this sense, the sweep rate was time-varying, and the number of data points available differed from field to field. We used InSb detectors, which were fast enough to generate a response within the order of 100 ns (~100 ns), and the ESR was observed in the transmission setup. In addition, data were acquired via a fast digital memory with a high vertical resolution of 10 bits. A min-coil is a wounded copper wire with an inner diameter of 8 mm reinforced by the epoxy resin. As a mini-coil can be cooled down by liquid He in 5 min because of the small heating output, in principle one can achieve 12 shots in an hour, whereas only one up-and-down sweep is possible with a superconducting magnet. This sweep time efficiency is a big advantage of our mini-pulsed magnetic field system, especially for multi-frequency THz ESR measurements on

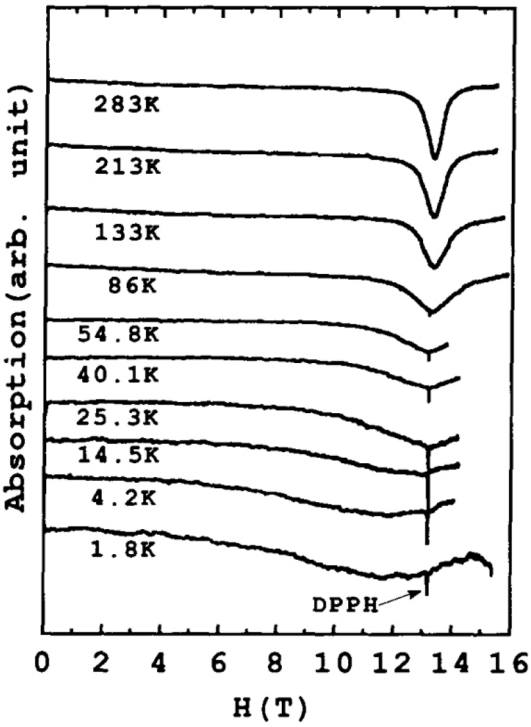

Fig. 4 Temperature dependence of $SrCr_8Ga_4O_{19}$ ESR absorption lines taken at 370.4 GHz [12]. DPPH is the standard for $g=2$. This is an example of advantage of THz ESR 5), the observation of ESR with the linewidth of several tesla at 1.8 K. Reprinted from Physica B: Condensed Matter, Vol. 201, M. Sumikawa, H. Ohta, M. Motokawa, H. Kikuchi and H. Nagasawa, "EPR of the Kagome antiferromagnet $SrCr_8Ga_4O_{19}$" /132–126., Copyright (1994) with permission from Elsevier

unknown samples. Although the spin sensitivity of our transmission type mini-pulsed magnetic field system described above is in the order of 10^{15} spins/G, it can be reduced dramatically to 10^{11} spins/G recently by using the microcantilever ESR under the pulsed magnetic field [24]. The selection between two methods depends on the amount of samples which can be used for the measurement. Typical examples of the multi-frequency THz ESR results using our transmission type mini-pulsed magnetic field system are shown in Figs. 1, 2 and 3 [3, 5, 10]. In addition, Figs. 6 and 7 [25] show results for $Y_2BaNi_{0.96}Mg_{0.04}O_5$. $Y_2BaNiMgO_5$ [26] is a typical model substance of the Haldane system [27], wherein the $S=1$ (Ni^{2+} ion in the case of $Y_2BaNiMgO_5$) one-dimensional antiferromagnet manifests the Haldane gap, distinguishing it from the $S=1/2$ one-dimensional antiferromagnet lacking such a gap [28]. The ground state of a Haldane chain can be well described by the Affleck–Kennedy–Leib–Tasaki model [29]. In this model, the $S=1$ state is described as two ferromagnetically aligned $S=1/2$ states, leading to a ground state corresponding to a valence-bond-solid (VBS) state where each $S=1/2$ forms a singlet with the nearest neighbor situated on the adjacent site (two red arrows surrounded by a blue curve in Fig. 8). This is purely a quantum effect in the $S=1$ one-dimensional antiferromagnet. When the two Ni^{2+} ions are replaced by the non-magnetic Mg^{2+} ions, two effective $S=1/2$ spins (green arrows in Fig. 8) appear at each end of the finite chain. As suggested by Batista et al. [30], two effective $S=1/2$ spins form a ferromagnetic dimer in the finite odd chain, resulting in a triplet ground state, whereas they form an antiferromagnetic

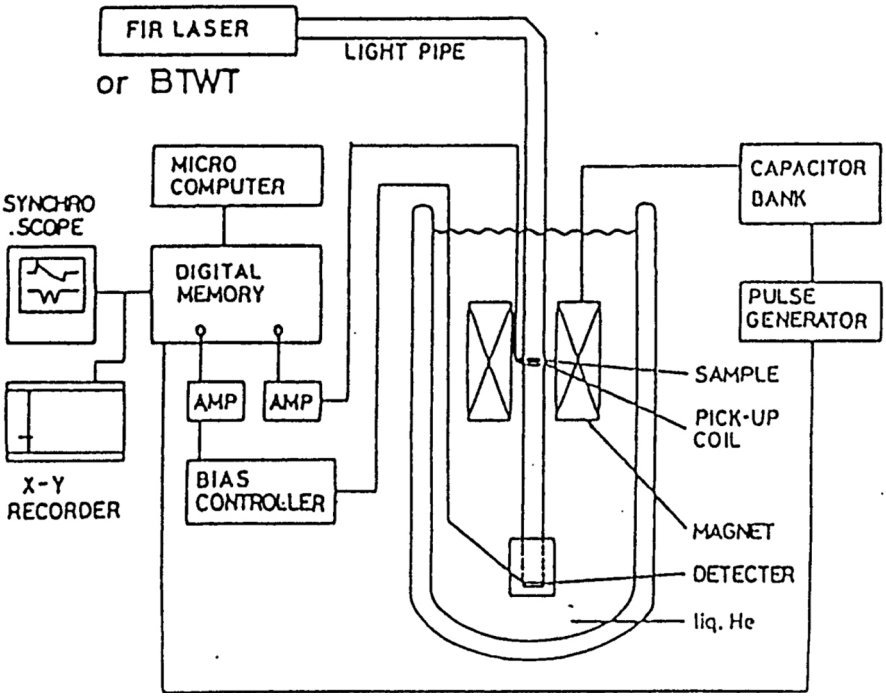

Fig. 5 Block diagram of our mini-pulsed magnetic field system which can produce up to 15 T [23]. The light sources are far-infrared (FIR) laser and backward traveling wave oscillators (BWO or BTWT) before 1995, and Gunn oscillators and multipliers became available after 1995. The detector is the liquid He cooled InSb. Reprinted from International Journal of Infrared and Millimeter Waves, 12(2), Mitsuhiro Motokawa et al., "Submillimeter EPR of Co:Rb_2MgF_4 and anomalous g values"/149, Copyright (1991) with permission from Springer Nature

dimer in the finite even chain, leading to a singlet ground state, as shown in Fig. 8. Therefore, the triplet ground state (odd chain) exhibits stronger ESR at very low temperatures. Moreover, as suggested by Batista et al. [30], there are effective D and E terms determined based on the N-length of the finite chain. Here, N corresponds to the number of Ni ion sites in the finite chain. These D and E terms diminish as N increases due to the reduced correlation between the two effective $S = 1/2$ spins. The N-dependent effective D and E terms cause multiple secondary ESR peaks to emerge, as shown in Figs. 6 and 7. For $N >> 1$, two free $S = 1/2$ spins produce the main peak near DPPH, as shown in Fig. 6. The N dependence of the effective D and E terms yields insights into the spin correlation within the Haldane system [25]. In summary, Figs. 1, 2, 3, 6 and 7 underscore the power of multi-frequency THz ESR measurements using the mini-pulsed magnetic field.

On the other hand, there are cases where THz ESR measurements beyond 15 T are necessary when dealing with magnetic systems characterized by exchange interactions. A 55 T pulsed magnetic field THz ESR system was developed in Kobe, incorporating a 300 kJ (10 kV) capacitor bank and a reinforced Cu–Ag

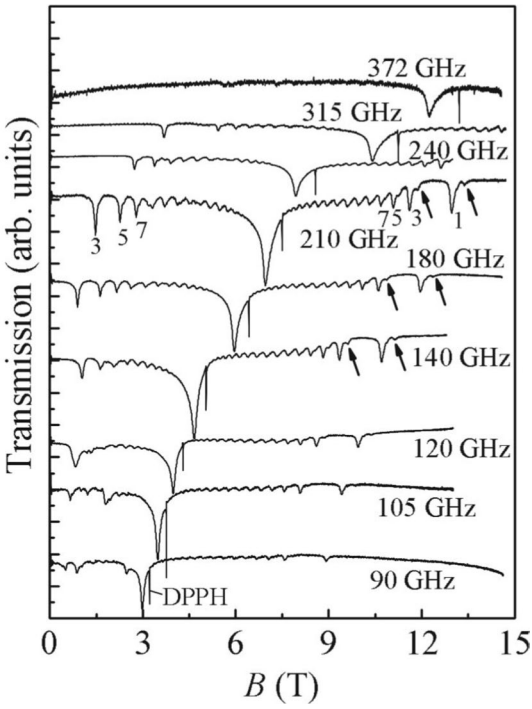

Fig. 6 ESR spectra of $Y_2BaNi_{0.96}Mg_{0.04}O_5$ single crystal for various frequencies at 4.2 K in the magnetic field B parallel to the *c*-axis, where the Ni^{2+} chains run along the *a*-axis [25]. For example, the contributions of *N*-length chains are labeled $N (= 1, 3, 5, 7)$ for 210 GHz. Additional peaks indicated by arrows originate from a small domain whose *c*-axis slightly tilts from that for the main part of the sample. Reprinted Fig. 1 with permission from "Energy Structure of a Finite Haldane Chain in $Y_2BaNi_{0.96}Mg_{0.04}O_5$ Studied by High Field Electron Spin Resonance": M. Yoshida, K. Shiraki, S. Okubo, H. Ohta, T. Ito, H. Takagi, M. Kaburagi, and Y. Ajiro, Phys. Rev. Let, 95, 117–202 and 2005. Copyright (2005) by the American Physical Society

wire pulsed magnet [31]. Although this magnet is cooled by liquid N_2, it takes more than 30 min to cool the magnet after a 55 T shot because of the high heating output coming from the high current is greater than that from a mini-coil. Therefore, the data acquisition efficiency becomes much lower than in the case of the mini-coil, but it opens up the possibility for high-field THz ESR measurements beyond the capabilities of a conventional superconducting magnet. Sample temperatures hover around the liquid He temperature because low temperatures are a constant necessity for investigating the ground states of the magnetic systems. The multifrequency 55 T pulsed magnetic field THz ESR system is especially useful for exploring magnetic field phases at high fields beyond the magnetic phase transition point H_m. Figure 9 illustrates a typical example, displaying the frequency-field diagram of $Cu_3(CO_3)_2(OH)_2$ (Azurite) observed at 1.8 K for H///b, revealing magnetic phase transitions at 16 T and 26 T [32]. Azurite is a deformed diamond chain antiferromagnet whose ground state is in the spin liquid phase [32, 33]. Utilization of only natural mineral single crystals is viable to Azurite, as laboratory growth conditions are inadequate for its production. Furthermore, the material exhibits a very anisotropic 1/3 magnetization plateau, an uncommon trait for the Cu^{2+} ion [33]. The Dzyaloshinskii–Moriya interaction has been proposed as a candidate, yet the underlying cause of the anisotropic 1/3 magnetization plateau remains incompletely understood [34]. The magnetic field range between 16 and 26 T corresponds to the 1/3 magnetization plateau region observed in the magnetization measurements at 1.5 K for H//b. Mode D in Fig. 9 is essentially the

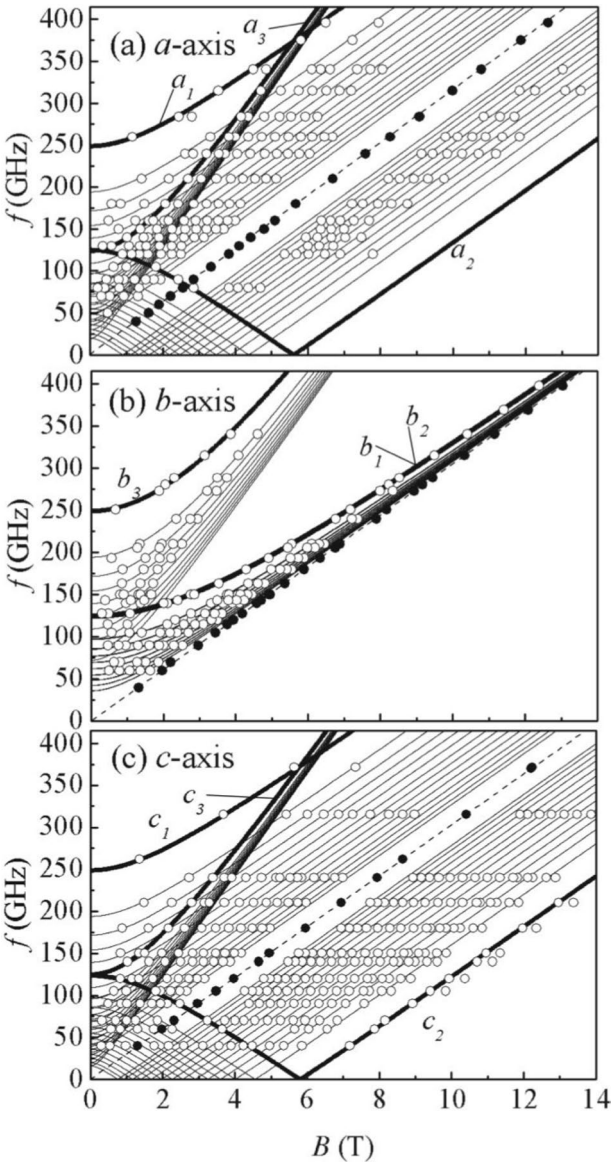

Fig. 7 Frequency-field diagrams of $Y_2BaNi_{0.96}Mg_{0.04}O_5$ single crystal for the applied field B along different directions **a** B//a, **b** B//b, and **c** B//c. The solid and open circles represent the resonance points for the main peak and secondary peaks, respectively. The dashed lines indicate the resonance modes for free $S = 1/2$ spins [25]. Here, labeling a, b and c correspond to crystal axes, and 1, 2 and 3 correspond to different ESR modes coming from the zero-field splitting of the triplet ground states in odd chain explained in Fig. 8. Reprinted Fig. 2 with permission from "Energy Structure of a Finite Haldane Chain in $Y_2BaNi_{0.96}Mg_{0.04}O_5$ Studied by High Field Electron Spin Resonance": M. Yoshida, K. Shiraki, S. Okubo, H. Ohta, T. Ito, H. Takagi, M. Kaburagi, and Y. Ajiro, Phys. Rev. Let, 95, 117–202 and 2005. Copyright (2005) by the American Physical Society

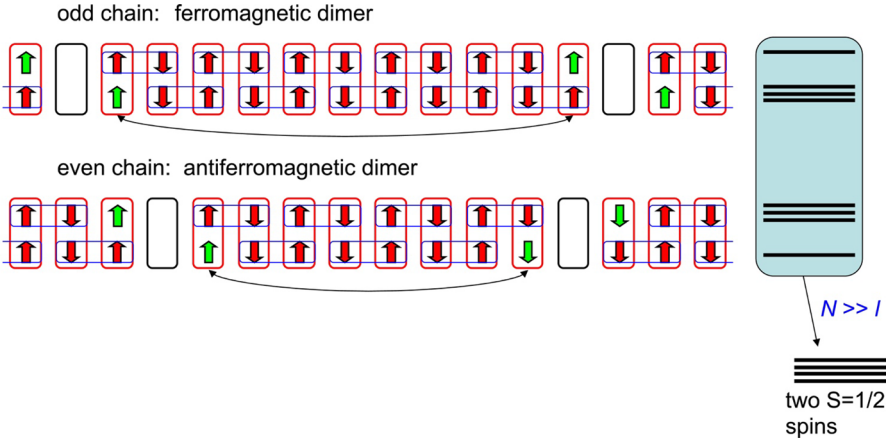

Fig. 8 Schematic diagrams of the finite odd chain and the finite even chain based on the VBS state (left), and corresponding energy states are shown (right). The effective D term and E term in the triplet ground state of ferromagnetically coupled effective $S=1/2$ spins (green arrows) will decrease as the N-length increases, and it will give different ESR modes in Fig. 7. See text for the details (Color figure online)

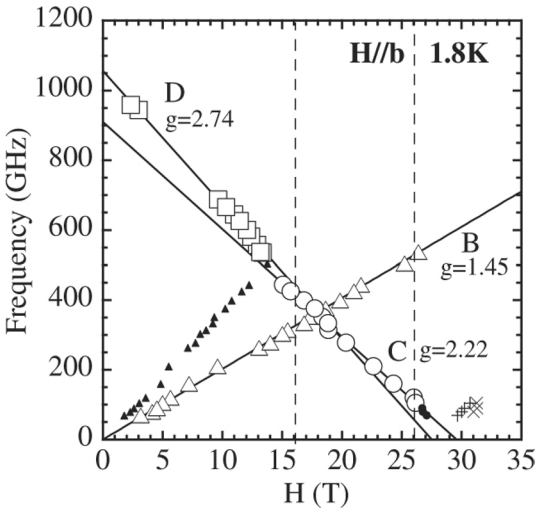

Fig. 9 Frequency-field diagram of $Cu_3(CO_3)_2(OH)_2$ (Azurite) observed at 1.8 K for H///b. The major resonances B, C and D are written in large symbols, while the minor resonances are written in small symbols [32]. The field range between 16 and 26 T corresponds to the 1/3 magnetization plateau region observed in the magnetization measurement at 1.5 K [33]. The slope change in mode C suggests a change in the spin state within the 1/3 magnetization plateau phase. Reproduced with permission from Ref. [32]. **c** (2003) The Physical Society of Japan

downward transition of the triplet state of the $S=1/2$ dimer under the influence of the magnetic field. However, its slope changes to mode C around 16 T, suggesting a change in the spin state within the 1/3 magnetization plateau phase. A similar outcome was obtained through inelastic neutron measurements conducted after 5 years under a magnetic field [35], suggesting also the advantage of high-field THz ESR due to its ability to utilize much smaller single crystals compared to neutron measurements. Finally, similar THz ESR using the pulsed magnetic field

beyond 50 T is available at the Dresden High Magnetic Field Laboratory [36] and the Center for Advanced High Magnetic Field Science, Osaka University [37].

3 Mechanically Detected THz ESR

It has been shown that the use of small mechanical devices [38] such as micro-cantilever and nano-membrane allows highly sensitive detection in magnetic resonance measurements. Such mechanically detected magnetic resonance techniques were pioneered by Sidles [39] and Rugar [40], and its sensitivity finally reached at the level of single electron spin detection [41]. One of promising applications is magnetic resonance force microscopy (MRFM) [42–44], where the spatial distribution of electron and nuclear spins in solids can be visualized with high spatial resolution. It should be noted that the frequency range of these applications is in the microwave region to achieve high spatial resolution and high sensitivity. On the other hand, we focused on the use of micromechanical devices in the sub-THz and THz regions, where high-sensitive ESR measurements have been difficult due to the lower irradiation power.

Mechanically detected THz ESR technique has been developed in our group since 2006 [20, 45]. In this technique, small mechanical devices are used to detect ESR signals, instead of the standard bolometric detectors. At the ESR transition, electron spins in the down-spin state are excited to the up-spin state by absorbing THz waves. This absorption process is accompanied by a magnetization change of the system because the population between the down-spin and up-spin states is changed. In mechanically detected ESR technique, this magnetization change is converted to a field-gradient force or a magnetic torque exerting on the mechanical devices. The advantage of this technique is the enhanced sensitivity to a small-volume sample on the order of micrograms, which has been very difficult to measure in the THz region. As examples of cantilever-detected ESR in the THz region, we have reported ESR detection beyond 1 THz [46] and in situ sample-rotating ESR apparatus in the THz region [47]. In this review, we focus on mechanically detected THz ESR using membrane devices.

A membrane device is a kind of mechanical structure made of a thin plate, the perimeter of which is fixed to the substrate. Compared to micro-cantilever devices, the lateral dimensions are larger, and typically are on the order of millimeters. Though the vibrational modes are rather complicated, we only consider the fundamental mode, known as the drum mode corresponding to uniform deformation of the membrane. Several types of nano-membranes are commercially available. We show here the piezoresistive membrane (model SD-MSS-1 K supplied by NanoSensors) and the ultrathin SiN_x nanomembrane (model MEM-N03001/7.5 M supplied by NTT AT). The dimensions of the former membrane are 1 mm in diameter and 5.2 μm in thickness, while those for the latter are 3×3 mm in size and 100 nm in thickness.

Shown in Fig. 10a is a photo of the piezoresistive membrane used in this study [48]. The membrane device was applied to THz ESR measurements [49], in a similar manner to the piezoresistive micro-cantilever. Two types of detection modes,

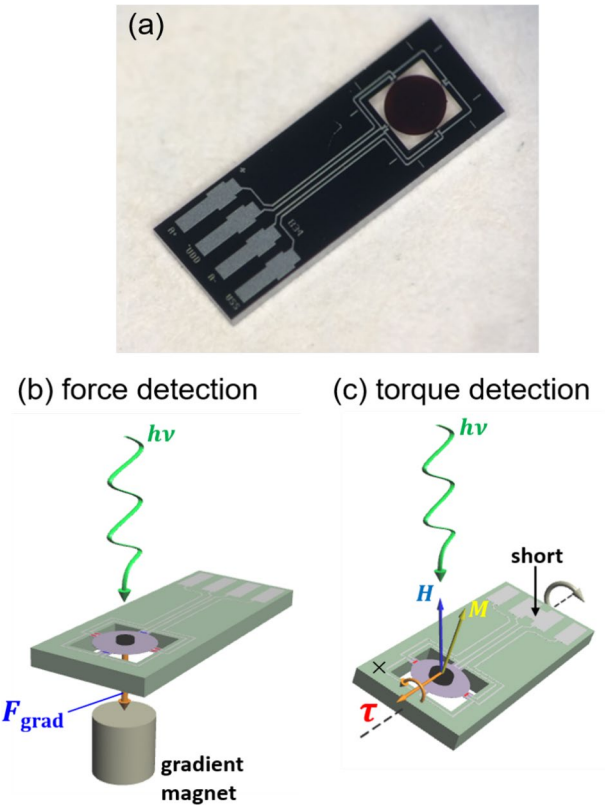

Fig. 10 **a** Photo of a commercially available piezoresistive membrane. Four piezoresistive paths for monitoring the membrane deformation are fabricated at the perimeter. Two detection modes of a commercially available piezoresistive membrane: **b** field-gradient force detection and **c** torque detection. The former is used for magnetically isotropic samples such as powder samples, combined with a field-gradient magnet placed below the membrane. On the other hand, the latter is used for magnetically anisotropic single crystals

field-gradient force and torque, were possible, as shown in Fig. 10b, c. In the force mode, the membrane deforms uniformly, whereas in the torque mode it is twisted along the rotation axis. The users can select most suitable detection modes depending on types of the sample used. Using the piezoresistive membrane, we successfully performed THz ESR spectroscopy of Co Tutton salt, $Co(NH_4)_2(SO_4)_2 \cdot 6H_2O$ [49], which is a paramagnetic salt with a large magnetic anisotropy arising from Co^{2+} ions.

Much better sensitivity was obtained using the SiN_x nano-membrane due to the thinner thickness [19, 22]. Figure 11a shows a schematic of the nano-membrane assembly in the force mode. In this setup, a small gradient magnet was mounted at the center of the nano-membrane, and the sample was mounted on a thin metal plate just above the gradient magnet. This "magnet-on-membrane" configuration has a couple of the following advantages: First, once the gradient magnet is glued

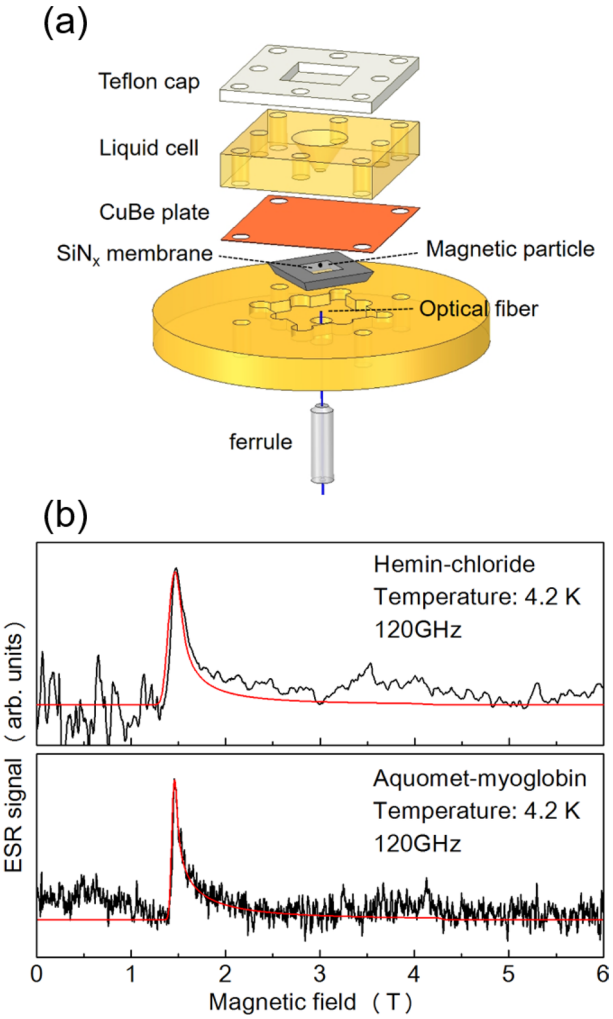

Fig. 11 **a** Schematic of the experimental setup for mechanically detected THz ESR for solution samples. A magnet-mounted nanomembrane was embedded on a brass plate, and its deformation could be sensitively monitored by a fiber-optic Fabry–Perot interferometer. A conical brass cell was placed above the thin metal plate for solution samples. The cell was sealed with a PTFE plate. The sample volume was typically 5–10 μL. **b** ESR signals of frozen solutions of hemin chloride (upper trace) and aquomet–myoglobin (lower trace) observed at 120 GHz. Fitted results are indicated by red curves (Color figure online)

to the membrane, samples can be quickly and easily exchanged without touching the fragile nano-membrane. Second, the thin metal plate plays a role of shielding the sample and membrane from incident THz waves. This setup helps to reduce the degrading effects of the incident THz waves such as ferromagnetic resonance of the gradient magnet itself and spurious mechanical excitations. When the ESR condition is satisfied, the magnetic force acting between the sample and the gradient magnet is changed. This change in turn produces a uniform deformation of

the magnet-on-membrane, which is sensitively measured by a fiber-optic interferometer placed beneath the membrane. In this setup, a conical brass container was used to mount a solution sample on the thin plate [22]. The container was capped with a PTFE plate, which is highly transparent to THz waves.

Figure 11b shows the ESR spectra of frozen solution samples of hemin chloride (upper trace) and aquomet–myoglobin (lower trace) observed at 4.2 K [22]. For hemin, the sample concentration and volume were 50 mM and 5 μL (2.5×10^{-7} mol), respectively. For myoglobin, on the other hand, they were 8.8 mM and 10 μL(8.8×10^{-8} mol), respectively. Myoglobin is a kind of hemoprotein, and its molecular weight is about 17 kDa. The functional role is oxygen storage in muscle, and its active center has the same local structure as hemin chloride, except that both sides of the porphyrin ring are coordinated by a water molecule and a histidine residue for aquomet–myoglobin. In both measurements, asymmetric spectra were clearly observed at 120 and 210 GHz. The observed signals are attributed to ferric ions in the high-spin state (Fe^{3+}, $S=5/2$), where the g factor ranges between 2 and 6 in the heme environment. The overall ESR lineshape was explained by orientational average of the randomly oriented frozen

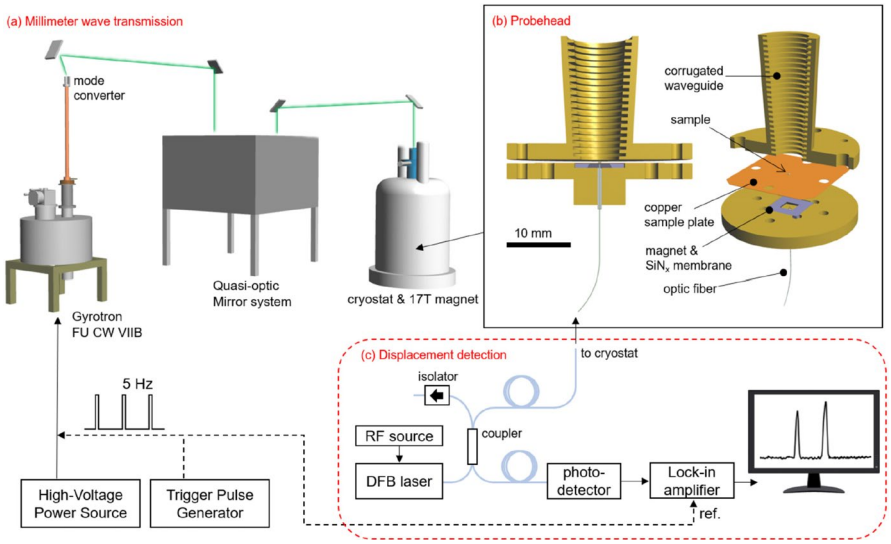

Fig. 12 **a** Schematic of the mechanically detected THz ESR system using a gyrotron source. The gyrotron was driven at 154.088 GHz by trigger pulses with a repetition rate of 5 Hz with variable duty ratios. The output beam was transmitted to the sample cryostat in the free space using the quasi-optic mirror system. **b** Cross-sectional view of the probe head used in this study. The incident beam was propagated from the top of the cryostat to the sample space via a corrugated waveguide. A sample was placed on a thin metal plate, below which a magnet-mounted-nanomembrane was placed for ESR detection. **c** Setup of optical interferometry for the displacement measurement of the nanomembrane. A fiber-optic Fabry–Perot interferometer was used for detection of the ESR-induced membrane deformation. A DFB laser was used as a light source of the interferometer, and the back-reflected light from the membrane was measured by a photodetector. The synchronous signals with the repetition frequency were monitored using a lock-in amplifier. Reprinted with permission from [30]. Copyright 2018 AIP Publishing

solution sample. These asymmetric signals were well reproduced by simulation curves with appropriate parameters.

As shown in Fig. 12, we recently combined our mechanically detected THz ESR system with a high-power source, gyrotron, to further increase the sensitivity [50]. Gyrotron is a kind of vacuum tube oscillators based on the cyclotron motion of electrons inside the cavity placed in a magnetic field. We used the gyrotron source (FU CW VIIB) developed at the University of Fukui. It was operated at 154.088 GHz in the pulse mode with a repetition rate of 5 Hz and a duty ratio of $D = 0.1$–10%. Therefore, the peak and average power of the incident wave at the sample space were estimated to be $P_{peak} = 5$ W and $P_{av} = 5$–500 mW, respectively. The incident waves were introduced through a PTFE window into the cryostat and were irradiated on the sample after propagation through the 1-m-long circular corrugated waveguide. In our setup, the signals were obtained as a change of the sample magnetization during irradiation cycles. Therefore, the peak power is responsible for the signal amplitude, and hence the signal-to-noise ratio. In this sense, the use of high-power gyrotron sources has a superior advantage over solid-state devices.

For the test samples, we used 20 μg of DPPH powder and a $Cu(C_4H_4N_2)(NO_3)_2$ (CuPzN) single crystal with dimensions of $0.8 \times 0.5 \times 0.08$ mm^3. DPPH is an organic free radical compound that is widely used as an ESR standard. CuPzN is a one-dimensional quantum spin chain material with a very low Neel temperature of $T_N = 107$ mK. We extended the temperature region of mechanically detected ESR measurement to higher region and successfully observed ESR signals near room temperature at 280 K, as shown in Fig. 13a. This result shows the advantage of the high-power radiation source. The performance of our system was also demonstrated

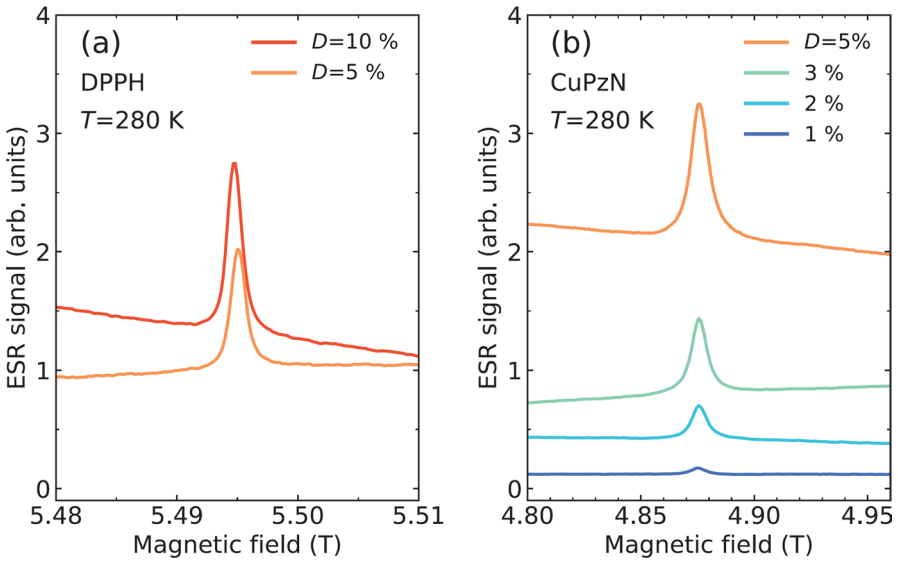

Fig. 13 Mechanically detected THz ESR spectra of **a** DPPH powder and **b** CuPzN single crystal with different duty ratios (D) at $T = 280$ K. It is noted that the data for CuPzN showed larger absorption widths, as D increased. Reprinted with permission from [50]. Copyright 2018 AIP Publishing

by the measurement of CuPzN single crystals with a broader linewidth than DPPH (Fig. 13b). The baseline at 280 K was found to have a linear slope, which is related to the thermal drift of the interferometer tuning. We recently succeed in multi-frequency ESR measurements in a wide frequency up to 400 GHz using the single gyrotron source, FU CW CII, installed at the University of Fukui, which allowed multi-frequency radiation using different cavity modes between 108 and 397 GHz. The peak power at the output port was 439, 251, and 18.8 W for 135.4, 186.6, and 394 GHz, respectively. Therefore, high-sensitive THz ESR spectroscopy at room temperature will be made possible in the near future.

4 High Pressure THz ESR

We present examples of high pressure ESR measurements in the THz region in this section. In X-band, since the first ESR measurement under pressure in 1957 [51], various techniques were developed to improve pressure range, sensitivity and so on. A system having a diamond anvil cell with a gasket which also works as a resonator achieved a pressure of 10 GPa (1985) [52], and a combination of an anvil cell and dielectric resonators achieved a sensitivity of about one-third that of the conventional rectangular cavity TE_{102} mode (2005) [53]. Around 2000 the focus of development has shifted to ones using high magnetic field and high frequency. Among them are a system combining a piston–cylinder pressure cell with a quasi-optical system [54], and a system combining a millimeter vector network analyzer with a plastic diamond anvil cell [55]. While the high sensitivity is one of the features for these two high pressure ESR systems, our systems are oriented towards the higher frequency range with ensuring the signal-to-noise ratio with the larger sample space. The most important key of our high pressure ESR system

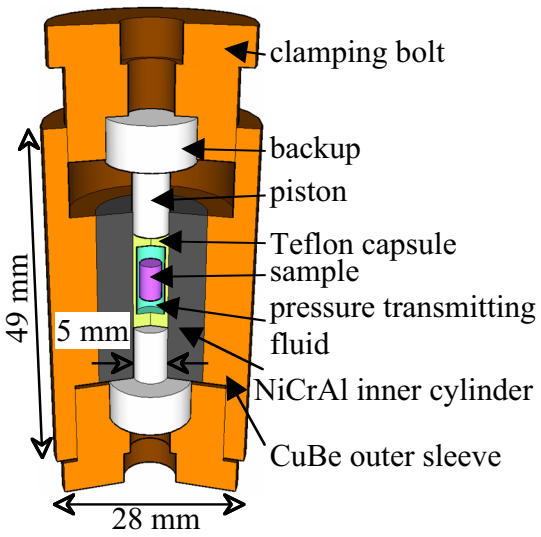

Fig. 14 Cross section of THz wave transmission type pressure cell [17]. The cylinder consists of an inner NiCrAl cylinder and a CuBe outer sleeve. The upper and bottom backups and pistons are all made of ZrO_2-based ceramics. Reprinted with permission from [17]. Copyright 2015 Elsevier

is a THz wave transmission type pressure cell (Fig. 14) [17]. The design of the pressure cell is based on a double-layer piston–cylinder type one, which is widely used in solid-state physics. However, all internal parts of our pressure cell are made of ZrO_2-based ceramics, whereas those of the same type of pressure cell are usually made of metal. The ZrO_2-based ceramics has both proper transmission to THz waves and mechanical toughness. This allows irradiation of THz waves to the sample subjected to pressure and observation of the transmission intensity. The sample space is about 10 mm height with an inner diameter of 5 mm or 4 mm, and can generate hydrostatic pressures of up to 2.5 GPa [17] and 2.8 GPa [56], respectively. The relatively large sample space provides a sufficient signal-to-noise ratio. Some of our developments of high pressure ESR system and its applications are summarized in the reviews [57, 58].

Pressure is the only means to control the exchange interactions and the magnetic anisotropy acting on the spins of magnetic materials cleanly and continuously, and our high pressure THz ESR is a promising tool to observe novel phenomena arising from these changes [18, 59–65]. In spin gap systems composed of $S=1/2$ antiferromagnetic dimers, the ratio J'/J of the interdimer interaction(s) J' to the intradimer interaction J can be varied by the pressure [18, 64]. Here we present a result of the spin gap compound $KCuCl_3$ [64], which undergoes a phase transition from a gapped disordered state to a three-dimensional ordered state as J'/J increases by pressure. In our high pressure THz ESR measurement of this system, the Higgs amplitude mode, which is an excitation mode peculiar to spin gap systems, was confirmed just above the critical pressure. We also show a newly developed high pressure ESR technique, where we detect ESR calorimetrically [66], and its application to another spin gap compound Cu_2(1,4-diazacycloheptane)$_2Cl_4$ (CuHpCl).

$KCuCl_3$ is isostructural to a well-known $S=1/2$ spin dimer compound $TlCuCl_3$. The ground state and the first excited state of this system is the nonmagnetic singlet state ($S=0$) and the triplet state ($S=1$), respectively, and it is known to exhibit the field-induced order [67] and the pressure-induced order [68], which are typical of the spin gap system. Since the ESR signals due to the direct transition from $S=0$ to $S_z=\pm1$ of $S=1$ were observed, the energy difference between the ground state and the first excited state at zero field was accurately determined. Although such direct transition is forbidden in ESR, it was shown that the vector spin chirality on dimer plays an important role in making the transition probability finite [69]. Figure 15a shows the pressure dependence of the gap energy determined from the direct transition ESR modes. Two excitations corresponding to wavenumbers $\boldsymbol{k}=(0,0,0)$ (A-mode) and $(0,0,2\pi)$ (B-mode) were observed, which reflects the presence of two types of dimers in the unit cell. The pressure dependence of the gap energy directly obtained in this measurement is in good agreement with the results of the ESR measurement at ambient pressure [70], the magnetization (M) measurement [68] and the inelastic neutron scattering (INS) measurement [71]. By analyzing the pressure dependence of the gap energy, the critical pressure P_c was obtained to be 0.82 GPa. Moreover, the pressure dependences of the intra- and interdimer interactions were determined and both were found to decrease with pressure. However, the decrease rate for the intradimer interaction is almost twice as much as that of the

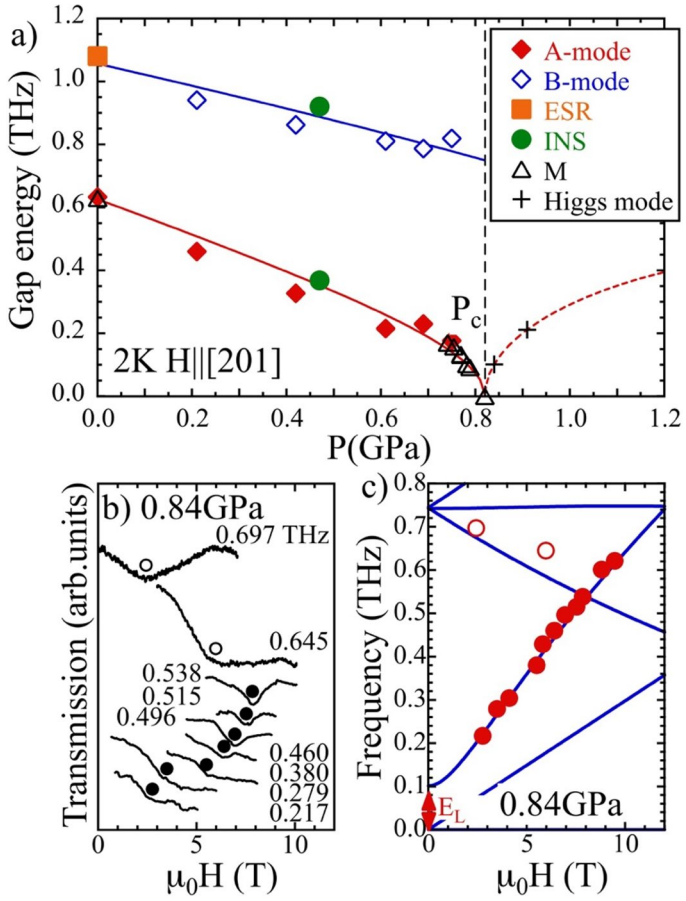

Fig. 15 Pressure dependence of gap energy obtained from the direct transition ESR A- and B-mode at 2 K, H||[201] (**a**). Data obtained from ESR at ambient pressure [70], INS measurements [71], and magnetization measurements (M) [68] are also plotted. The solid lines are the fitting results of the theoretical curves. The dotted line shows the pressure dependence of the excitation energy for the Higgs amplitude mode calculated theoretically using the results obtained below P_c. Frequency dependence of the spectra obtained at $P = 0.84$ GPa $> P_c$, 2 K, H||[201] (**b**), and its frequency–magnetic field diagram (**c**). The solid lines are the magnetic field dependence of the excitation energy calculated by the extended spin wave theory using the pressure dependence of the exchange interactions determined below P_c and assuming that it has the same pressure dependence above P_c. E_L represents the excitation energy corresponding to the cross mark at 0.84 GPa in (**a**). See ref. [64] for details. Reprinted with permission from [64]. Copyright 2022 Springer

sum of the interdimer interactions, which results in the increase in the ratio J'/J with pressure.

The gap closes at P_c and the system undergoes the phase transition to the long-range ordered state at sufficiently low temperature. Figure 15b shows the ESR spectra obtained at 2 K just above the critical pressure. As shown in the figure, the signal was successfully observed over a wide frequency range. In the pressure induced

ordered state of the spin gap system, in general, the quantum fluctuation contributes to the ordered moment significantly in the vicinity of the critical pressure. Therefore, an excitation mode corresponding to its longitudinal fluctuation along the moment, or the Higgs amplitude mode, is expected to appear [64]. This is an excitation mode that hardly can be observed in the ordinary antiferromagnet. Figure 15c shows its frequency field diagram. The solid lines show the calculated results by the extended spin wave theory using the pressure dependences of the intra- and interdimer interactions obtained below P_c. It shows good agreement with the experimental results. Thus, the pressure dependence of the gap energy was obtained in this system, and the Higgs amplitude mode was successfully observed by our high pressure THz ESR.

Next, we show a recently developed high pressure ESR technique. In ESR, excited spins release energy when they relax, and the released energy is eventually converted to heat. Therefore, the resonance can be observed by detecting the temperature increase of a sample. The excited spins transfer their energy to the lattice by the spin–lattice relaxation time T_1. Under the continuous wave condition, the temperature of the sample connected to the heat bath reaches a steady state with a time constant $\tau = C/K$, where C is the heat capacity of the sample and K is the thermal conductivity between the sample and the heat bath. Since T_1 is on the order of microseconds for many solid crystals [72, 73], the condition of $\tau >> T_1$ usually holds when K is small. Therefore, the temperature rise of the sample can be observed in a measurement with a timescale which is longer than τ. Alternatively,

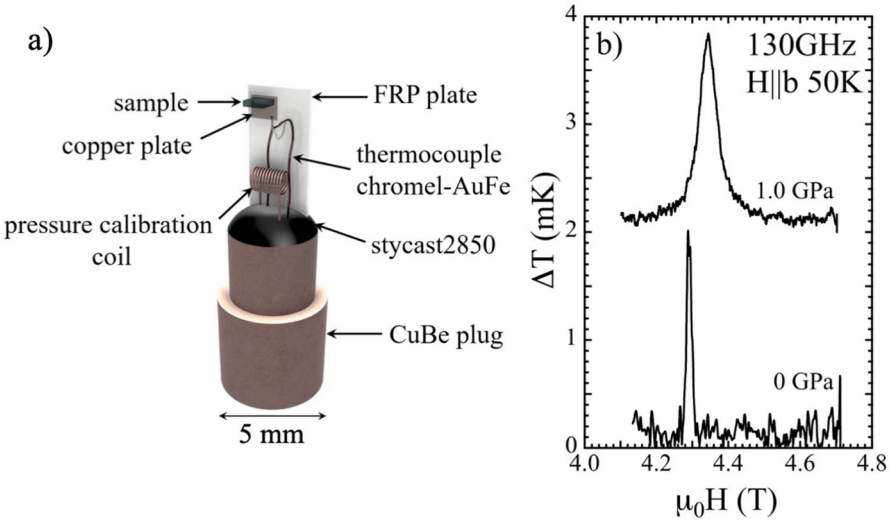

Fig. 16 Schematic diagram of sample setting for thermally detected high pressure ESR (**a**). The sample is glued to a copper plate on the FRP plate, and the temperature of the sample is measured by a chromel–AuFe thermocouple through the copper plate. The pressure in the sample space is calibrated by the superconducting transition temperature of tin in a pressure calibration coil. Thermally detected ESR spectra obtained at 0 GPa and 1.0 GPa for CuHpCl at 130 GHz, H||b and 50 K (**b**). The base line is shifted for clarity

the technique of AC calorimetry [74] can also be used. When we use the amplitude modulating electromagnetic wave with an appropriate period ω whose reciprocal satisfies the condition of $T_1 < \omega^{-1} < \tau$, the temperature of the sample reaches a steady state at a certain quantity proportional to $(\omega C)^{-1}$, and its temperature can be observed. Our group has demonstrated the thermally detected ESR in the THz region [75] and successfully applied this method to the measurement under pressure [66]. Figure 16a shows a setup around the sample. Instead of the lower piston shown in Fig. 14, the plug in Fig. 16a is set. A sample and one junction of AuFe-Chromel thermocouple is glued to a copper plate fixed to a fiber reinforced plastics (FRP) plate, where they are thermally connected through the copper plate, and the reference junction of the thermocouple is in the pressure medium. The temperature difference ΔT between the sample and the reference is measured by the ac calorimetric technique. Since the electromagnetic wave only needs to irradiate the sample, the bottom parts made of metal can be used. This enables us to introduce an ac coil as well as the thermocouple through an electrical feedthrough of the plug and the backup, and precise pressure calibration based on the pressure dependence of the superconducting transition of Sn is also utilized [76].

As an example of the application of this technique, we present a result of an $S = 1/2$ spin gap material CuHpCl. Although the temperature and field dependences of magnetization of this system are typical of spin gap system, the magnetic network is still controversial [77]. We found that a large change in the magnetic network occurs about 0.7 GPa from the magnetization measurements under pressure [78]. Figure 16b shows the thermally detected ESR spectra obtained at 0 and 1.0 GPa in the paramagnetic state. As shown in the figure, the ESR signal was very clearly observed. The temperature increase was about 2 mK in this experimental condition, and it depends on the conditions and changes up to about 100 mK. We found the resonance field shift to the higher field side and the line broadening by applying the pressure, and the g value changes from 2.165 to 2.139. The change in g value in the paramagnetic state suggests a change in the crystal field of the magnetic ion. On the other hand, no clear crystal structure change was observed under pressure [79], which implies that only the magnetic network changes while the crystal symmetry is preserved. By the combination with a split pair magnet we succeeded in obtaining the field angle dependent ESR spectra [75], and we plan to conduct this ESR measurement under pressure for this system. Further detailed information about the change in the magnetic network under pressure will be obtained in the near future.

5 Summary

Multi-extreme THz ESR system developed in Kobe is reviewed. After introducing the advantages of THz ESR in contrast to the conventional X-band ESR, three aspects of multi-extreme THz ESR, which are the pulsed magnetic field, the mechanical detection and high-pressure THz ESR measurements, are discussed. The measurement efficiency of 15 T mini-pulsed magnetic field THz ESR compared to the use of super conducting magnet is discussed with the multi-frequency results of hemin, Li_2CuO_2, $CsCuCl_3$ and the finite Haldane chain substance $Y_2BaNi_{0.96}Mg_{0.04}O_5$. As

an advantage of 55 T pulsed magnetic field THz ESR, the study of magnetic phase transitions in deformed diamond chain antiferromagnet $Cu_3(CO_3)_2(OH)_2$ (Azurite) is shown. Mechanically detected THz ESR using the nano-membrane device has the advantage of highly sensitive THz ESR of the order of micrograms. The THz ESR results of frozen solutions of hemin chloride and aquomet–myoglobin observed at 120 GHz are discussed as examples. Furthermore, the mechanically detected THz ESR results of DPPH powder and CuPzN single crystal at 280 K using a high power gyrotron are also introduced. Finally, the high-pressure THz ESR results of dimer antiferromagnet $KCuCl_3$ using the transmission-type double layered pressure cell are discussed. Moreover, the recent development of thermally detected high-pressure THz ESR is also shown with the example of CuHpCl. In summary we hope that this review will convince the readers about the power and the future of multi-extreme THz ESR.

Author Contributions HO, EO, and TS wrote the main manuscript text and HO and SO prepared Figs. 1, 2, 3, 4, 5, 6, 7, 8, and 9, EO and HT prepared Figs. 10, 11, 12 and 13, TS prepared Figs. 14, 15 and 16. All authors reviewed the manuscript.

Funding Open Access funding provided by Kobe University. Not applicable.

Data Availability No datasets were generated or analysed during the current study.

Declarations

Conflict of Interest The authors declare no competing interests.

Ethical Approval Not applicable.

References

1. B. Ferguson, X.-C. Zhang, Nat. Mater. **1**, 26 (2002)
2. H. Ohta, S. Okubo, K. Kawakami, D. Fukuoka, Y. Inagaki, T. Kunimoto, Z. Hiroi, J. Phys. Soc. Jpn. (2003). https://doi.org/10.1143/JPSJS.72SB.26
3. T. Okamoto, E. Ohmichi, S. Okubo, H. Ohta, J. Phys. Soc. Jpn. **87**, 013702 (2018)
4. E. Ohmichi, T. Okamoto, T. Sakurai, H. Takahashi, S. Okubo, H. Ohta, Appl. Mag. Res. **51**, 1103 (2020)
5. H. Ohta, N. Yamauchi, T. Nanba, M. Motokawa, S. Kawamata, K. Okuda, J. Phys. Soc. Jpn. **62**, 785 (1993)
6. W. Palme, F. Mertens, O. Born, B. Lüthi, U. Schotte, Solid State Commun. **76**, 873 (1990)
7. H. Tanaka, U. Schotte, K.D. Schotte, J. Phys. Soc. Jpn. **61**, 1344 (1992)

8. M. Motokawa, J. Phys. Soc. Jpn. (1978)
9. H. Nojiri, Y. Tokunaga, M. Motokawa, J. Phys. **49**(Suppl. C8), 1459 (1988)
10. H. Ohta, S. Imagawa, M. Motokawa, H. Tanaka, J. Phys. Soc. Jpn. **62**, 3011 (1993)
11. T. Nikuni, H. Shiba, J. Phys. Soc. Jpn. **62**, 3268 (1993)
12. M. Sumikawa, H. Ohta, M. Motokawa, H. Kikuchi, H. Nagasawa, Physica B **201**, 123 (1994)
13. H. Ohta, T. Sakai, Appl. Mag. Res. **52**(4), 263–564 (2021)
14. H. Ohta, S. Okubo, E. Ohmichi, T. Sakurai, W.-M. Zhang, T. Shimokawa, J. Low Temp. Phys. **170**, 511 (2013)
15. T. Sakurai, A. Taketani, T. Tomita, S. Okubo, H. Ohta, Y. Uwatoko, Rev. Sci. Inst. **78**, 065107 (2007)
16. K. Fujimoto, T. Sakurai, S. Okubo, H. Ohta, K. Matsubayashi, Y. Uwatoko, K. Kudo, Y. Koike, Appl. Mag. Res. **44**, 893 (2013)
17. T. Sakurai, K. Fujimoto, R. Matsui, K. Kawasaki, S. Okubo, H. Ohta, K. Matsubayashi, Y. Uwatoko, H. Tanaka, J. Mag. Res. **259**, 108 (2015)
18. T. Sakurai, Y. Hirao, K. Hijii, S. Okubo, H. Ohta, Y. Uwatoko, K. Kudo, Y. Koik, J. Phys. Soc. Jpn. **87**, 033701 (2018)
19. H. Takahashi, T. Okamoto, K. Ishimura, S. Hara, E. Ohmichi, H. Ohta, Rev. Sci. Instrum. **89**, 083905 (2018)
20. H. Ohta, M. Kimata, S. Okubo, E. Ohmichi, T. Osada, AIP Conf. Proc. **850**, 1643 (2006)
21. E. Ohmichi, N. Mizuno, M. Kimata, H. Ohta, Rev. Sci. Instrum. **79**, 103903 (2008)
22. T. Okamoto, H. Takahashi, E. Ohmichi, H. Ishikawa, Y. Mizutani, H. Ohta, Appl. Phys. Lett. **113**, 223702 (2018)
23. M. Motokawa, H. Ohta, N. Makita, Int. J. Infrared Milli Waves **12**(2), 149 (1991)
24. E. Ohmichi, N. Mizuno, M. Kimata, H. Ohta, T. Osada, Rev. Sci. Instrum. **80**, 013904 (2009)
25. M. Yoshida, K. Shiraki, S. Okubo, H. Ohta, T. Ito, H. Takagi, M. Kaburagi, Y. Ajiro, Phys. Rev. Lett. **95**, 117202 (2005)
26. J. Darriet, L.P. Regnault, Solid State Commun. **86**, 409 (1993)
27. F.D. Haldane, Phys. Rev. Lett. **50**, 1153 (1983)
28. J. des Cloizeaux, J.J. Pearson, Phys. Rev. **128**, 2131 (1962)
29. I. Affleck, T. Kennedy, E.H. Lich, H. Tasaki, Phys. Rev. Lett. **59**, 799 (1987)
30. C.D. Batista, K. Hallberg, A.A. Aligia, Phys. Rev. B **60**, R12554 (1999)
31. H. Ohta, M. Tomoo, S. Okubo, T. Sakurai, M. Fujisawa, T. Tomita, M. Kimata, T. Yamamoto, M. Kawauchi, K. Kindo, J. Phys. Conf. Ser. **51**, 611 (2006)
32. H. Ohta, S. Okubo, T. Kamikawa, T. Kunimoto, Y. Inagaki, H. Kikuchi, T. Saito, M. Azuma, M. Takano, J. Phys. Soc. Jpn. **72**, 2464 (2003)
33. H. Kikuchi, Y. Fujii, M. Chiba, S. Mitsudo, T. Sakai, T. Kuwai, H. Ohta, Phys. Rev. Lett. **94**, 227201 (2005)
34. H. Ohta, J. Phys. Soc. Jpn. **92**, 081003 (2023)
35. K.C. Rule, A.U.B. Wolter, S. Süllow, D.A. Tennant, A. Brühl, S. Köhler, B. Wolf, M. Lang, J. Schreuer, Phys. Rev. Lett. **100**, 117202 (2008)
36. S.A. Zvyagin, E. Cizmar, M. Ozerov, J. Wosnitza, R. Feyerherm, S.R. Manmana, F. Mila, Phys. Rev. B **83**, 060409(R) (2011)
37. T. Fujita, H. Yamaguchi, S. Kimura, T. Kashiwagi, M. Hagiwara, K. Matan, D. Grohol, D.G. Nocera, Y.S. Lee, Phys. Rev. B **85**, 094409 (2012)
38. A.N. Cleland, *Foundations of nanomechanics* (Springer, Berlin, 2003)
39. J.A. Sidles, Appl. Phys. Lett. **58**, 2854 (1991)
40. D. Rugar, C.S. Yannoni, J.A. Sidles, Nature **360**, 563 (1992)
41. D. Rugar, R. Budakian, H.J. Mamin, B.W. Chui, Nature **430**, 329 (2004)
42. J.A. Sidles, J.L. Garbini, K.J. Bruland, D. Rugar, O. Züger, S. Hoen, C.S. Yannoni, Rev. Mod. Phys. **67**, 249 (1995)
43. M. Poggio, C.L. Degen, Nanotechnology **21**, 342001 (2010)
44. S. Kuehn, S.A. Hickman, J.A. Marohn, J. Chem. Phys. **128**, 052208 (2008)
45. E. Ohmichi, T. Okamoto, H. Takahashi, H. Ohta, Appl. Mag. Reson. **52**, 283 (2021)
46. H. Takahashi, E. Ohmichi, H. Ohta, Appl. Phys. Lett. **107**, 182405 (2015)
47. E. Ohmichi, S. Hirano, H. Ohta, J. Mag. Reson. **227**, 9 (2013)
48. H. Takahashi, K. Ishimura, T. Okamoto, E. Ohmichi, H. Oha, J. Phys. Soc. Jpn. **86**, 063002 (2017)
49. H. Takahashi, K. Ishimura, T. Okamoto, E. Ohmichi, H. Ohta, Rev. Sci. Instrum. **89**, 036108 (2018)

50. H. Takahashi, Y. Ishikawa, T. Okamoto, D. Hachiya, K. Dono, K. Hayashi, T. Asano, S. Mitsudo, E. Ohmichi, H. Ohta, Appl. Phys. Lett. **118**, 022407 (2021)
51. W.M. Walsh Jr., N. Bloembergen, Phys. Rev. **107**, 904 (1957)
52. N. Sakai, J.H. Pifer, Rev. Sci. Instrum. **56**, 726 (1985)
53. A. Sienkiewicz, B. Vileno, S. Garaj, M. Jaworski, L. Forró, J. Magn. Reson. **177**, 261 (2005)
54. B. Náfrádi, R. Gaál, A. Sienkiewicz, T. Fehér, L. Forró, J. Magn. Reson. **195**, 206 (2008)
55. A. Prescimone, C. Morien, D. Allan, J.A. Schlueter, S.W. Tozer, J.L. Manson, S. Parsons, E.K. Brechin, S. Hill, Angew. Chem. Int. Ed. **51**, 7490 (2012)
56. T. Sakurai, Y. Yasutani, H. Segawa, S. Okubo, H. Ohta, Appl. Magn. Reson. **53**, 763 (2022)
57. T. Sakurai, S. Okubo, H. Ohta, J. Magn. Reson. **280**, 3 (2017)
58. T. Sakurai, H. Ohta, S. Hara, Y. Saito, Appl. Magn. Reson. **52**, 267 (2021)
59. T. Okamoto, E. Ohmichi, Y. Sito, T. Sakurai, H. Ohta, J. Phys. Chem. B **122**, 6880 (2018)
60. S.A. Zvyagin, D. Graf, T. Sakurai, S. Kimura, H. Nojiri, J. Wosnitza, H. Ohta, T. Ono, H. Tanaka, Nat. Commun. **10**, 1064 (2019)
61. R. Okuto, E. Ohki, T. Sakurai, K. Hijii, H. Takahashi, E. Ohmichi, S. Okubo, H. Ohta, Y. Uwatoko, H. Tanaka, Appl. Magn. Reson. **50**, 1059 (2019)
62. T. Sakurai, B. Rubrecht, L.T. Corredor, R. Takehara, M. Yasutani, J. Zeisner, A. Alfonsov, S. Selter, S. Aswartham, A.U.B. Wolter, B. Büchner, H. Ohta, V. Kataev, Phys. Rev. B **103**, 024404 (2021)
63. D. Yamamoto, T. Sakurai, R. Okuto, S. Okubo, H. Ohta, H. Tanaka, Y. Uwatoko, Nat. Commun. **12**, 4263 (2021)
64. M. Matsumoto, T. Sakurai, Y. Hirao, H. Ohta, Y. Uwatoko, H. Tanaka, Appl. Magn. Reson. **52**, 523 (2021)
65. K.Y. Povarov, D.E. Graf, A. Hauspurg, S. Zherlitsyn, J. Wosnitza, T. Sakurai, H. Ohta, S. Kimura, H. Nojiri, V.O. Garlea, A. Zheludev, A. Paduan-Filho, M. Nicklas, S.A. Zvyagin, Nat. Commun. **15**, 2295 (2024)
66. N. Nagasawa, T. Sakurai, H. Takahashi, E. Ohmichi, H. Ohta, J. Jpn. Soc. Infrared Sci. Technol. **32**, 72 (2022). (**in Japanese**)
67. A. Oosawa, T. Takamasu, K. Tatani, H. Abe, N. Tsujii, O. Suzuki, H. Tanaka, G. Kido, K. Kindo, Phys. Rev. B **66**, 104405 (2002)
68. K. Goto, M. Fujisawa, H. Tanaka, Y. Uwatoko, A. Oosawa, Y. Osakabe, K. Kakurai, J. Phys. Soc. Jpn. **75**, 064703 (2006)
69. S. Kimura, M. Matsumoto, M. Akaki, M. Hagiwara, K. Kindo, Phys. Rev. B **97**, 140406 (2018)
70. S. Kimura, K. Kindo, H. Tanaka, Phys. B **346–347**, 15 (2004)
71. K. Goto, T. Osakabe, K. Kakurai, Y. Ywatoko, A. Oosawa, J. Kawakami, H. Tanaka, J. Phys. Soc. Jpn. **76**, 053704 (2007)
72. D. Bourdel, G. Ablart, J. Pescia, S. Clement, J.P. Renard, Phys. Rev. B **23**, 1339 (1981)
73. K. Furukawa, T. Hara, T. Nakamura, J. Phys. Soc. Jpn. **79**, 043702 (2010)
74. A. Demuer, C. Marcenat, J. Thomason, R. Calemczuk, B. Salce, P. Lejay, D. Braithwaite, J. Flouquet, J. Low. Tmep. Phys. **120**, 245 (2000)
75. H. Takahashi, T. Sakurai, E. Ohmichi, H. Ohta, Rev. Sci. Instrum. **92**, 083901 (2021)
76. K. Kawasaki, T. Sakurai, E. Ohmichi, S. Okubo, H. Ohta, K. Matsubayashi, Y. Uwatoko, Appl. Mag. Reson. **46**, 987 (2015)
77. J. Jornet-Somoza, F. Cosi, M. Fumanal, M. Deumal, Dalton Trans. **50**, 1754 (2021)
78. T. Sakurai, R. Takehara, N. Nagasawa, H. Takahashi, M. Saga, K. Takahashi, S. Okubo, J. Phys. Soc. Conf. Proc. **38**, 011145 (2023)
79. T. Tajiri, H. Deguchi, M. Mito, S. Takagi, J. Phys. Soc. Jpn. **75**, 044708 (2006)